nanomaterials

MDPI

Article

Controlled Growth of WO_3 Photoanode under Various pH Conditions for Efficient Photoelectrochemical Performance

Seung-Je Yoo, Dohyun Kim and Seong-Ho Baek *

Department of Energy Engineering, Dankook University, Cheonan 31116, Republic of Korea; ysj3802@gmail.com (S.-J.Y.); kimoh422@gmail.com (D.K.)
* Correspondence: seongho@dankook.ac.kr

Abstract: Herein, the effects of the precursor solution's acidity level on the crystal structure, morphology, nucleation, and growth of $WO_3 \cdot nH_2O$ and WO_3 nanostructures are reported. Structural investigations on $WO_3 \cdot nH_2O$ using X-ray diffraction and Fourier–transform infrared spectroscopy confirm that the quantity of hydrate groups increases due to the interaction between H^+ and water molecules with increasing HCl volume. Surface analysis results support our claim that the evolution of grain size, surface roughness, and growth direction on $WO_3 \cdot nH_2O$ and WO_3 nanostructures rely on the precursor solution's pH value. Consequently, the photocurrent density of a WO_3 photoanode using a HCl-5 mL sample achieves the best results with 0.9 mA/cm^2 at 1.23 V vs. a reversible hydrogen electrode (RHE). We suggest that the improved photocurrent density of the HCl-5 mL sample is due to the efficient light absorption from the densely grown WO_3 nanoplates on a substrate and that its excellent charge transport kinetics originate from the large surface area, low charge transfer resistance, and fast ion diffusion through the photoanode/electrolyte interface.

Keywords: tungsten trioxide; tungsten trioxide hydrate; photoanode; water splitting; green hydrogen

Citation: Yoo, S.-J.; Kim, D.; Baek, S.-H. Controlled Growth of WO_3 Photoanode under Various pH Conditions for Efficient Photoelectrochemical Performance. *Nanomaterials* **2024**, *14*, 8. https://doi.org/10.3390/nano14010008

Academic Editor: Nikolaos Dimitratos

Received: 22 November 2023
Revised: 15 December 2023
Accepted: 18 December 2023
Published: 19 December 2023

1. Introduction

As the climate crisis has been aggravated because of the excessive use of fossil fuels, the demand for green and renewable energy has steadily increased worldwide [1]. As a result, it is crucial to secure carbon-free energy resources to meet the growing energy consumption. Green hydrogen production is an efficient way of generating high energy density, clean, and storable fuel [2,3]. One of the promising methods of achieving green hydrogen is to adopt a photoelectrochemical route that operates without an external bias [4–7].

Tungsten trioxide hydrates ($WO_3 \cdot nH_2O$, n = 0.33, 1, or 2) and tungsten trioxides (WO_3) have been widely investigated due to their diverse crystal structures and intriguing electrochemical and photovoltaic properties [8–20]. In particular, WO_3 has been considered as a promising semiconductor material for water splitting applications via a photoelectrochemical method, because it is stable and non-toxic, and its band gap is also suitable for visible light absorption [12,14,16,21–23]. In general, $WO_3 \cdot nH_2O$ has been prepared through the solution-phase synthesis, and the WO_3 has been obtained after removing water molecules from $WO_3 \cdot nH_2O$ using calcination processes [24–26]. Thus, many efforts have been exerted on $WO_3 \cdot nH_2O$ and WO_3 nanostructures to develop suitable preparation methods for efficient photoelectrode applications, including acid precipitation and a hydrothermal process, by controlling the morphology, crystal structure, and growth direction at room or moderate temperatures [14–21,27,28]. However, to the best of our knowledge, there has been no report on the relationship between the structural evolution of $WO_3 \cdot nH_2O$ and its effect on the electrochemical performance of WO_3 photoanodes while controlling the crystal structure of $WO_3 \cdot nH_2O$.

In the present study, we prepared $WO_3 \cdot nH_2O$ nanostructures by acid precipitation with various levels of hydrochloric (HCl) acid concentration and elucidated the influence

of the precursor solution's acidity level on the crystal structure, morphology, nucleation, and initial growth mode of the $WO_3 \cdot nH_2O$ samples. Furthermore, we investigated the relationship between the structural evolution of $WO_3 \cdot nH_2O$ nanostructures and their effect on the water oxidation properties of WO_3 photoanodes.

2. Experiments

2.1. Synthesis of $WO_3 \cdot nH_2O$ and WO_3 Materials

In order to improve the statistical significance of the results, three samples were prepared by repeating the following experimental procedure three times for each sample. Firstly, $WO_3 \cdot nH_2O$ was prepared by simple acid precipitation at room temperature with the following processes: 0.4 mmol of sodium tungstate dihydrate ($Na_2WO_4 \cdot 2H_2O$) was dissolved in 15 mL of deionized (DI) water and various amounts of 3 M HCl were dropped in the prepared solution while it was stirred. The samples obtained after adding each volume of HCl solution were labeled HCl-1 mL, HCl-2.5 mL, HCl-5 mL, HCl-7.5 mL, and HCl-10 mL, respectively. Then, 0.8 mmol of ammonium oxalate was dissolved in 15 mL of DI and added to the above solution with stirring to achieve the polymeric oxide. The prepared solution was poured into a Teflon-lined autoclave for hydrothermal synthesis at 140 °C for 3 h. Lastly, the as-grown $WO_3 \cdot nH_2O$ samples were rinsed with DI and ethyl alcohol several times, and WO_3 materials were obtained after they were calcined using a furnace at 500 °C in air for 2 h. The preparation procedures of $WO_3 \cdot nH_2O$ and WO_3 materials are presented as a schematic illustration in the Supplementary Materials (Figure S1).

2.2. Preparation of a WO3 Photoanode on Substrate

Fluorine-doped tin oxide (FTO) glass was used as a substrate cut to 2 cm x 2 cm and then cleaned by sequential sonication in ethyl alcohol, isopropyl alcohol, and DI water for 10 min in each solution. The cleaned FTO glass was vertically aligned on the jig and placed in the autoclave for the growth of the WO_3 film on the substrate. The detailed preparation procedures of the WO_3 photoanode on the FTO substrate are provided as an illustration in Figure S2.

2.3. Characterizations

The crystal structure was analyzed by X-ray diffraction (XRD, Miniflex 600) using a Cu Kα source. Fourier–transform infrared (FTIR, Perkin Elmer, Waltham, MA, USA) spectroscopy was adopted to study the chemical compositions. Surface analyses were conducted using scanning electron microscopy (SEM, Gemini II, Oberkochen, Germany) and atomic force microscopy (AFM, XE-100). The pH value of the solution was measured with a pH meter (HI2214, HANNA Instruments, Smithfield, RI, USA) which was calibrated with three kinds of pH buffer solutions for use in the high acidity condition. The pH controller was sequentially calibrated in pH 7, pH 4, and pH 1.68 buffer solutions (Thermo Scientific, Waltham, MA, USA). The acidity of the precursor suspension was varied within a wide pH range from 0.05 ± 0.01. to 1.12 ± 0.02 by adjusting the HCl volume. The names of the samples according to the HCl volume and average pH values for precursor suspensions are provided in Table 1. All electrochemical performances were measured with a three-electrode system using platinum as a counter electrode, Ag/AgCl as a reference electrode, and 0.5 M Na_2SO_4 (pH 6.9) used as an electrolyte. A Xenon lamp (LS150, ABET technologies) with a power of 150 W was used as the light source, and the illumination area of the photoanode was 2.54 cm^2. The light intensity of a solar simulator with an air mass (AM) 1.5 G filter was calibrated to a 1 sun condition (100 mW/cm^2) using a Si photodiode (RR_227 KG5, ABET technologies). And, the photoelectrochemical measurements on the WO_3 photoanode were conducted by using back-side illumination. An electrochemical workstation (Versastat3, Ametek) was used for linear scan voltammetry (LSV) measurements with a scan rate of 10 mV/s. Electrochemical impedance spectroscopy (EIS) was conducted in the frequency range from 1 MHz to 0.1 Hz with a 10 mV voltage amplitude. The obtained potential of the working electrode was converted into the potential of the reversible hydrogen electrode (RHE) using the following equation:

$$E_{RHE} = E_{Ag/AgCl} + 0.197 + 0.059\ pH$$

where E_{RHE} is the potential referred to for the RHE and $E_{Ag/AgCl}$ is the achieved potential against the Ag/AgCl (3 M KCl saturated) reference electrode.

Table 1. Average pH values of precursor solutions according to HCl volume.

Sample	HCl-1 mL	HCl-2.5 mL	HCl-5 mL	HCl-7.5 mL	HCl-10 mL
pH value	1.12 ± 0.02	0.86 ± 0.02	0.62 ± 0.01	0.34 ± 0.01	0.05 ± 0.01

2.4. Data Acquisition

To demonstrate the reproducibility of all the samples, XRD, LSV, and EIS data were obtained. Three samples with different HCl volumes were measured under the same condition and showed almost identical results as shown in the Supplementary Materials (Figures S3–S6); therefore, samples denoted as #1 among the replica were reported in the Results and Discussion section to provide their typical results.

3. Results and Discussion

Figure 1 illustrates the structural evolution of $WO_3 \cdot nH_2O$ by varying the HCl concentration during the acid precipitation process using Na_2WO_4 as a precursor, DI water as a solvent, and HCl solution as a precipitant. When HCl was introduced to Na_2WO_4, NaCl and tungstic acid (H_2WO_4) were generated by the following chemical reaction (1) [18]:

$$2HCl + Na_2WO_4 \rightarrow H_2WO_4 + 2NaCl \quad (1)$$

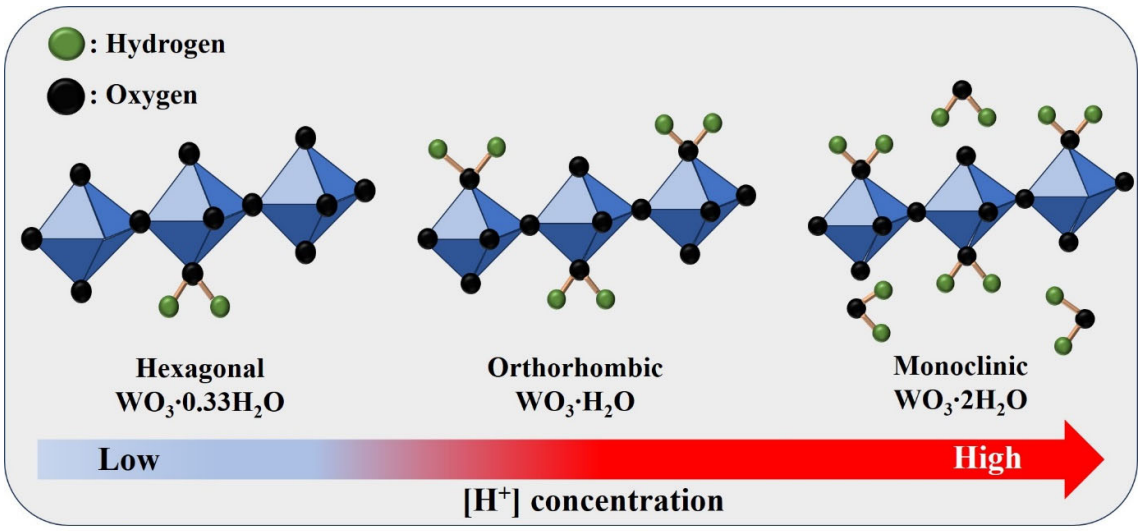

Figure 1. Schematic diagram of the $WO_3 \cdot nH_2O$ under various pH conditions during the acid precipitation process.

In general, H_2WO_4 can exist in the form of neutral $WO_2(OH)_2$. Under highly acidic conditions, namely, a high H^+ ion concentration and low pH value, nucleophilic water molecules tend to interact with $[WO_2(OH)_2]$ by the following reaction (2) [18,29,30]:

$$[WO_2(OH)_2] + 2H_2O \rightarrow [WO(OH)_4(OH_2)] \quad (2)$$

According to the above reaction, $WO(OH)_4(OH_2)$ metal complexes were developed, and the aggregation between adjacent octahedral $WO(OH)_4(OH_2)$ occurred in the form of corner-sharing. Moreover, the 2D stacked layers of $WO_3 \cdot H_2O$ and $WO_3 \cdot 2H_2O$ were gradually created with increasing interaction between seed $WO(OH)_4(OH_2)$ and water molecules owing to van der Waals forces [15,31].

According to the chemical reactions of (1) and (2), the structural change of the $WO_3 \cdot nH_2O$ caused by the H^+ concentration was clearly observed in the XRD patterns as shown in Figure 2. The XRD peaks of each sample corresponded to the hexagonal $WO_3 \cdot 0.33H_2O$ (JCPDS no. 35-1001), orthorhombic $WO_3 \cdot H_2O$ (JCPDS no. 43-0679), and monoclinic $WO_3 \cdot 2H_2O$ phases (JCPDS no. 18-1420). For the HCl-1 mL sample, 1 mL of HCl was added into a Na_2WO_4 solution during acid precipitation, and the hexagonal $WO_3 \cdot 0.33H_2O$ and orthorhombic $WO_3 \cdot H_2O$ phases developed because of the weak interaction between a low H^+ concentration and nucleophilic water molecules. However, the peak intensity at 22.9°, 24.3°, 26.9°, and 28.3° assigned to the lattice planes of (001), (110), (101), and (200) of the hexagonal structure greatly decreased with an increasing HCl volume, suggesting that the $WO_3 \cdot 0.33H_2O$ hexagonal phase transformed into the $WO_3 \cdot H_2O$ orthorhombic phase as shown in Figure 2b [32]. Likewise, Figure 2b clearly shows that the crystal structure of the HCl-7.5 mL and HCl-10 mL samples were transformed from the orthorhombic $WO_3 \cdot H_2O$ phase to the monoclinic $WO_3 \cdot 2H_2O$ phase owing to the promoted interaction of H^+ and water molecules leading to the formation of $WO_3 \cdot 2H_2O$. Furthermore, based on XRD measurements, we claim that the reproducibility of $WO_3 \cdot nH_2O$ can be demonstrated as shown in Figure S3. Therefore, we suggest that the crystal structure of $WO_3 \cdot nH_2O$ (n = 0.33, 1.00, or 2.00) can be precisely engineered by changing the volume of HCl precipitants during room temperature wet synthesis.

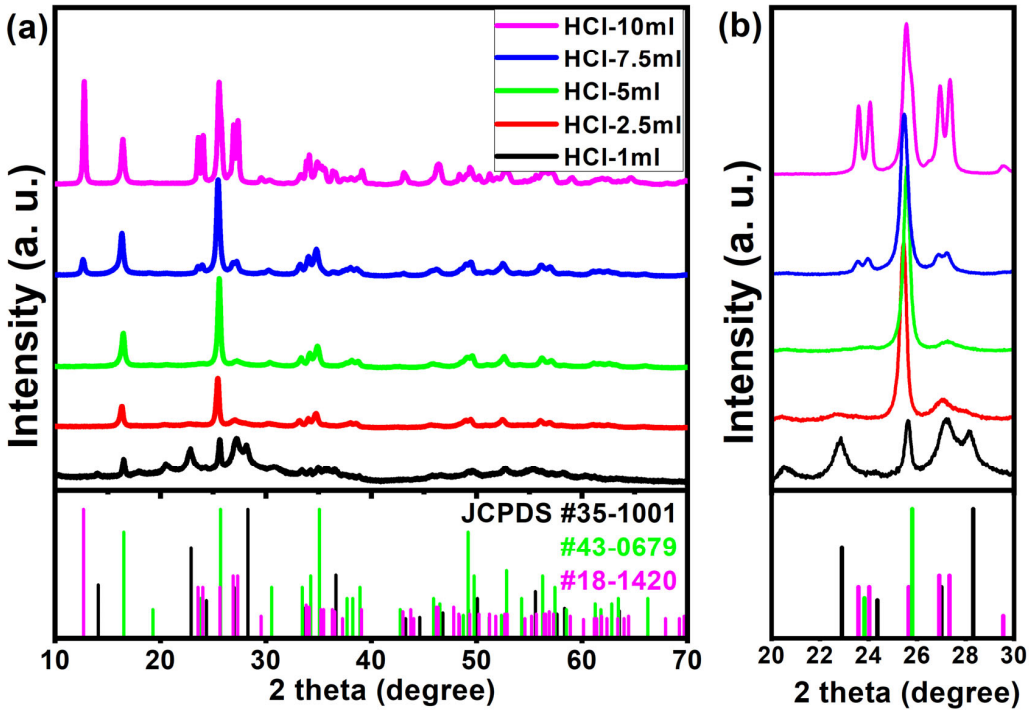

Figure 2. XRD spectra of the $WO_3 \cdot nH_2O$ powders obtained by an acid precipitation process. (**a**) 2theta range from 10° to 70° and (**b**) magnified XRD spectra in the 2theta range from 20° to 30°.

Figure 3 shows the FTIR spectra of the prepared $WO_3 \cdot nH_2O$ samples under different HCl concentrations. The absorption bands in the range of 500–1000 cm^{-1} are characteristic of the various WO_3 crystal lattices, i.e., W–O, O–W–O, and W=O bonds. The strong peak around 630 cm^{-1} was assigned as the stretching mode of metal–oxygen (O–W–O) [15,33]. In addition, the strong IR absorption observed at 945 cm^{-1} was due to the stretching mode of W=O bonds of hydrated WO_3 with an increasing H^+ concentration [33]. Two strong absorption peaks near 1610 and 3500 cm^{-1} arose from the H–O–H bending and O–H stretching vibrations of H_2O, respectively, suggesting that $WO_3 \cdot nH_2O$ can host a large number of water molecules either in the coordinated or interlayer form [33,34]. Thus, the FTIR results suggested that the quantity of hydrate groups increased due to the interaction

of H^+ and nucleophilic water molecules with an increasing HCl volume, which is consistent with the XRD results.

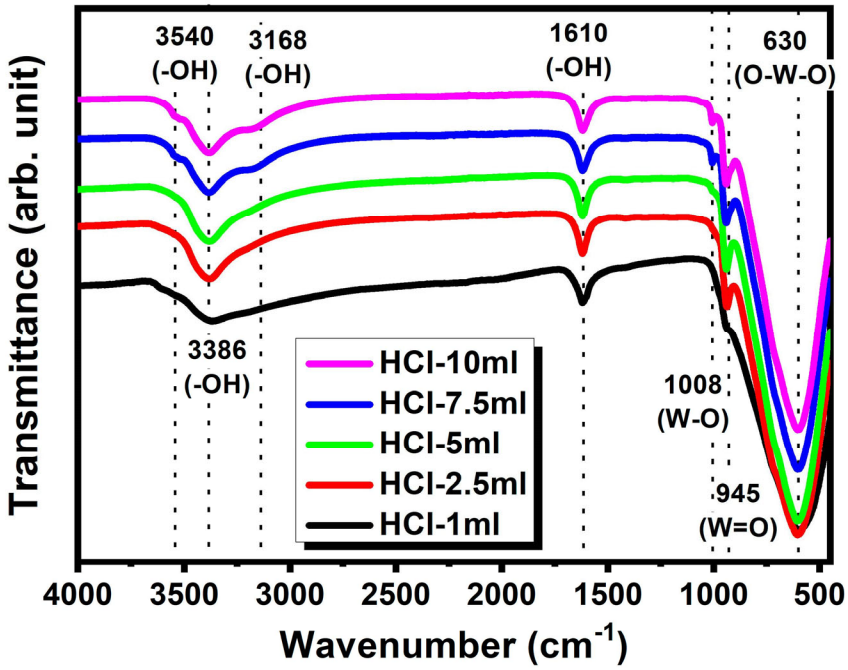

Figure 3. FTIR spectra of the $WO_3 \cdot nH_2O$ powders obtained by an acid precipitation process.

To elucidate the relationship between the crystal structure and the initial nucleation growth of the $WO_3 \cdot nH_2O$ on an FTO substrate, AFM was used to achieve three-dimensional (3D) images of all the samples. The 3D AFM images of the $WO_3 \cdot nH_2O$ nanostructures grown on FTO glass with different amounts of HCl during acid precipitation are presented in Figure 4. The AFM image of the bare FTO glass exhibits a smooth surface, while island-like grains can be observed for the samples with different HCl concentrations. The smooth surface of bare FTO glass exhibits a root mean square (RMS) of 38.4 nm (Figure 4a). However, as the amount of HCl increased during acid precipitation of $WO_3 \cdot nH_2O$ nanostructures, sharp grains developed on the surfaces of the FTO glass (Figure 4b–f). The size and RMS of these grains increased up to a HCl volume of 5 mL as shown in Figure 4b–d. Among the prepared samples, the HCl-5 mL sample shows higher values of RMS surface roughness, indicating that the growth rate of $WO_3 \cdot nH_2O$ nanostructures is the highest among the samples. In contrast, the growth rate of $WO_3 \cdot nH_2O$ was decreased in the samples prepared with 7.5 mL and 10 mL of HCl. The driving force for nucleation is closely related to the supersaturation of $WO(OH)_4(OH_2)$ seed molecules according to the chemical reaction of (2). At a larger pH value (low H^+ concentration), the number of WO_3 nuclei could be limited because of the small supersaturation of seed molecules. On the contrary, at a smaller pH value (high H^+ concentration), a great deal of nuclei could be quickly generated, due to the larger supersaturation of seed molecules. However, Pham et al. report that the condensed H^+ ion had a confining effect that generates a strong electric field, inhibiting long-ordered nucleation growth [18]. Therefore, the optimized nucleation growth of WO_3 nanoplates can be obtained in the moderate pH value and it is found to be the HCl-5 mL sample in our experimental results. Therefore, we suggest that the evolution of grain size, surface roughness, and inter-grain space distribution on $WO_3 \cdot nH_2O$ nanostructures rely on the precursor solution's acidity level.

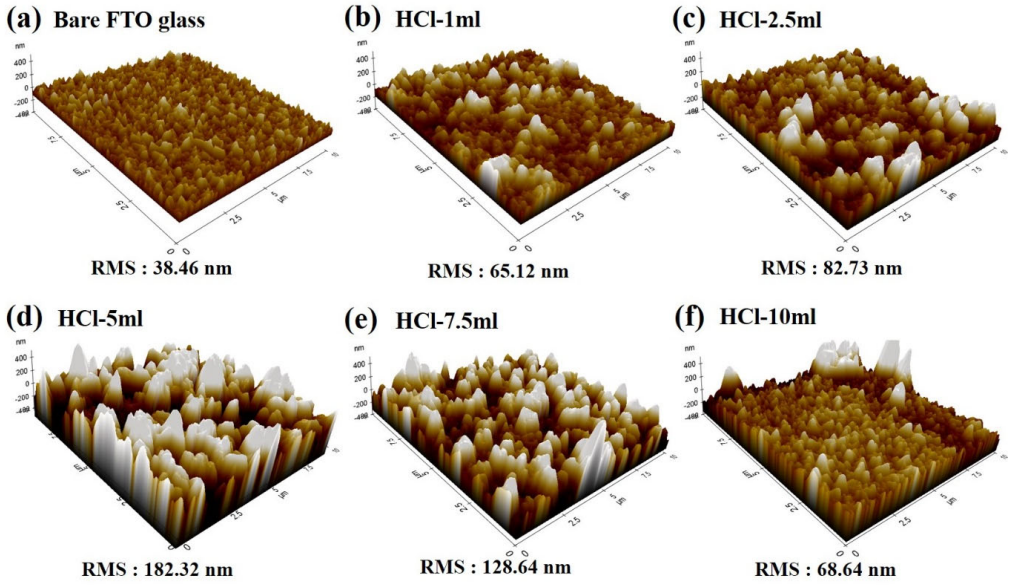

Figure 4. AFM images of the $WO_3 \cdot nH_2O$ powders grown on FTO substrates with different HCl volumes during acid precipitation.

After the hydrothermal growth and calcination process, $WO_3 \cdot nH_2O$ nanostructures can be dehydrated and transformed to achieve the WO_3 phase [26,27]. To study the crystal structure of WO_3 materials on FTO glass, we conducted the XRD measurements, and the diffraction results are provided in Figure 5a. Regardless of the $WO_3 \cdot nH_2O$ nanostructures and HCl concentration, the crystal structure of all the samples was identified as monoclinic WO_3 (JCPDS no.43-1035) after calcination [35]. It can be seen from Figure S4 that these results are demonstrated via repeated XRD measurements using a dummy sample. It should be noted that the peak intensity of the crystal plane gradually increased from the (002) to the (200) plane, as the HCl volume increased from 1 to 5 mL. The highest diffraction peak intensity of the crystal plane (200) was obtained from the WO_3 nanoplate on FTO glass with the incorporation of 5 mL of HCl as shown in Figure 5b.

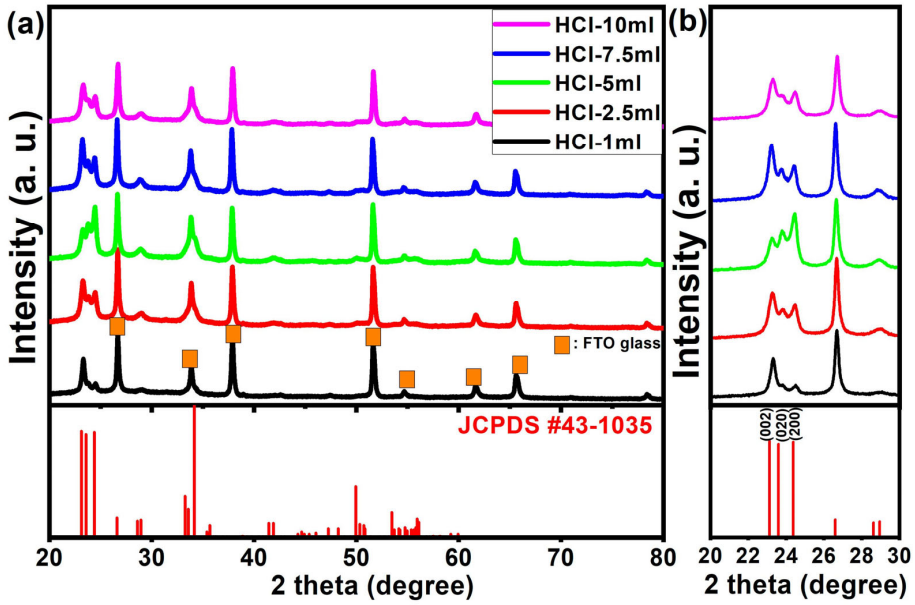

Figure 5. XRD results of the WO_3 nanoplates grown on FTO glass. (**a**) 2theta range from 20° to 80° and (**b**) magnified XRD spectra in the 2theta range from 20° to 30° (orange squares indicate the XRD peak positions of the FTO substrate).

Figure 6 shows the SEM images of the monoclinic WO_3 nanoplates grown on the FTO glass substrate after hydrothermal growth and the calcination process. The low-magnification top-view SEM images (Figure 6a–e) reveal that the HCl volume significantly affects the density of the WO_3 nanoplate. As the HCl was incorporated into the precursor solution, the density of the WO_3 nanoplates increased up to the HCl-5 mL sample; afterward, the density of the WO_3 nanoplates drastically decreased in the WO_3 nanoplates prepared with 7.5 mL and 10 mL of HCl, according to the AFM results as provided in Figure 4. Even though the WO_3 nanoplate samples prepared by 1 mL of HCl had the lowest density among all the samples, due to the low supersaturation of seed molecules, a high-magnification SEM image (Figure 6f) revealed that the largest WO_3 nanoplates were created by subsequent oxolation reactions on WO_3 nuclei. Meanwhile, as the HCl volume increases, the seed molecules become more supersaturated, which makes it possible to generate a lot of nuclei on the substrate. However, the condensed H^+ ion generates a strong electric field, inhibiting long-ordered nucleation and subsequent WO_3 nanoplate growth as shown in Figure 6j. These results support our claim that the crystal growth of the WO_3 nanoplate was greatly influenced by the initial nuclei density of $WO_3 \cdot nH_2O$ nanostructures on the substrate; therefore, the optimum pH value for the growth of WO_3 nanoplates should lie in the moderate pH range and it is revealed to be the HCl-5 mL sample as shown in Figure 6h. Figure 6k–o show the cross-sectional SEM images of the WO_3 nanoplates on the substrates. Vertically aligned WO_3 nanostructures with a length of 1–2 µm were well-grown on the FTO layer as indicated in Figure 6k. As confirmed from the magnified top-view SEM images, the largest WO_3 nanoplates were observed in the HCl-1 mL sample (Figure 6k). On the other hand, it should be noted that the rest four samples have a similar growth thickness, but they have a different density of WO_3 nanoplates. Moreover, we clearly observed that the growth direction of the WO_3 nanoplates changed from a slanted to a vertical direction for the substrates according to the proportion of the WO_3 nanoplates (Figure 6k–o). When the WO_3 nanoplates were sparsely distributed on the substrate under a low acidity level, they were grown on FTO glass with an inclined direction against the substrate. However, as the number of WO_3 nanoplates increased at high acidity levels, they densely grew on the substrate and the density of WO_3 nanoplates was maximized in the HCl-5 mL sample as shown in Figure 6m.

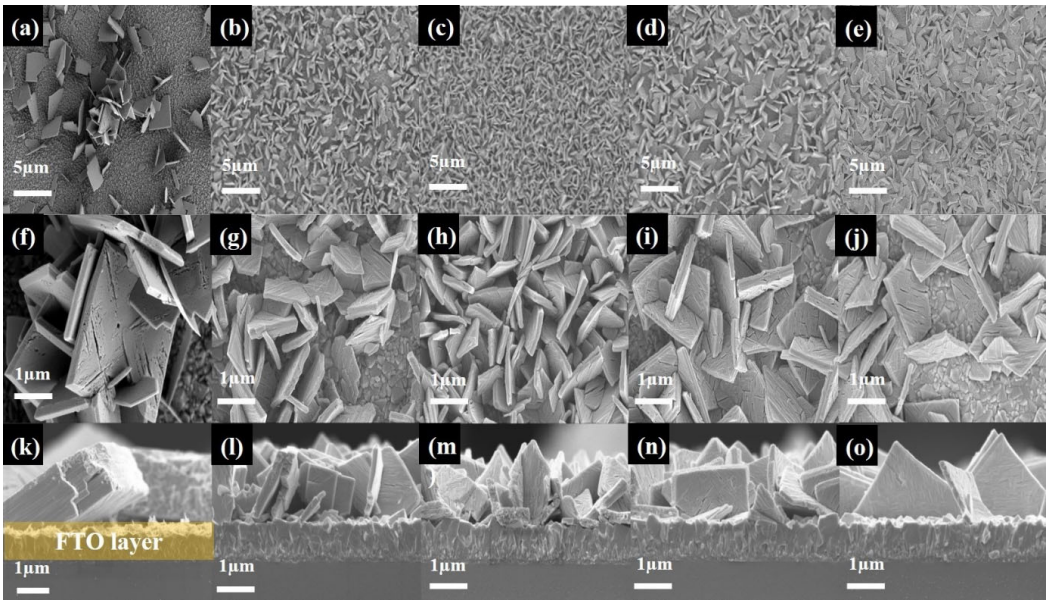

Figure 6. SEM images of the WO_3 nanoplates grown on FTO glass with different HCl volumes. (**a**) HCl-1 mL, (**b**) HCl-2.5 mL, (**c**) HCl-5 mL, (**d**) HCl-7.5 mL, (**e**) HCl-10 mL samples. Magnified (**f**–**j**) top-view and (**k**–**o**) cross-section view SEM images of the WO_3 nanoplates corresponding to the upper panel.

Consequently, the preferential growth direction of the WO_3 nanoplate changed according to the initial growth conditions, which resulted in a change in the strongest XRD peak from (002) to (200) as shown in Figure 5b. Thus, we claim that the HCl volume plays a crucial role in the growth process of $WO_3 \cdot nH_2O$ nanostructures and WO_3 nanoplates on FTO substrates.

The PEC performance of the prepared WO_3 photoanodes was investigated under AM 1.5 G conditions with an illuminated area of 2.54 cm^2. Figure 7 shows the LSV results of the WO_3 photoanodes with different amounts of HCl in a 0.5 M Na_2SO_4 electrolyte. According to the LSV curve, the dark currents of all the samples were less than 20 $\mu A/cm^2$ and were regarded as negligible. When the HCl concentration increased, the photocurrent density was enhanced as shown in Figure 7. The photocurrent density of the photoanode reached the highest value with 0.9 mA/cm^2 at 1.23 V vs. RHE for the HCl-5 mL sample, while that of the HCl-1 mL sample exhibited the lowest with 0.3 mA/cm^2 at the same voltage. However, as the incorporated amount of HCl further increased to more than 5 mL, the photocurrent densities decreased from 0.65 to 0.57 mA/cm^2 at 1.23 V vs. RHE for the WO_3 photoanodes prepared with 7.5 mL and 10 mL of HCl. As a result of repeated measurement using a replica, we suggest that the WO_3 photoanodes with different HCl volumes can be identically reproduced as shown in Figure S5. Therefore, we claim that the improved photocurrent is due to the enhanced light absorption from the dense and large volume of WO_3 nanoplates in a HCl-5 mL photoanode, which facilitates the charge transport kinetics by producing more photogenerated electron-hole pairs.

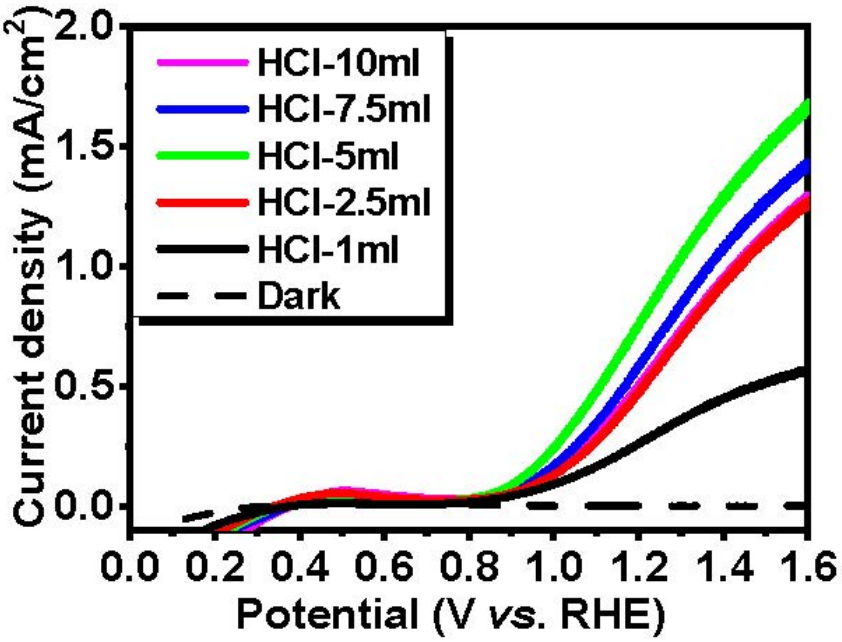

Figure 7. LSV curves obtained from the WO_3 photoanodes under AM 1.5 G conditions.

EIS measurements were conducted to prove the charge transfer kinetics at the WO_3 photoanodes–electrolyte interface. The EIS results are presented as a Nyquist plot at an open-circuit voltage under AM 1.5 G illumination as shown in Figure 8. As seen in Figure 8, the HCl-5 mL photoanode sample represents the smallest semicircle compared to the other electrodes, indicating a much lower photoelectrode–electrolyte interfacial resistance compared to the other electrodes [36]. In this work, the obtained EIS data were fitted into the RC circuit model as provided in the inset of Figure 8, containing a resistance and a capacitance in parallel. Because the water oxidation takes place at the WO_3 photoanode–electrolyte interface, the charge transfer resistance (R_{ct}) and double layer capacitance (CPE) can be observed at the interface [37,38]. The charge transfer resistances for all the samples were obtained by using the ZSimpWin software (version 3.21), and their

values for the HCl-1 mL, HCl-2.5 mL, HCl-5 mL, HCl-7.5 mL, and HCl-10 mL samples were 1445, 1372, 687, 987, and 2704 Ω, respectively. The fitting results clearly confirm that the derived R_{ct} values for the HCl-5 mL photoanode were the smallest among all the samples. From the results of EIS data for three samples under the same condition, we confirm that the reproducibility of photoanodes–electrolyte interfacial resistance can be demonstrated as shown in Figure S6. Therefore, we suggest that the superior PEC performance of the HCl-5 mL sample is attributed to the electrode–electrolyte accessibility of the WO_3 nanoplate owing to the densely grown nanostructure, efficient charge transfer, and fast ion diffusion between the photoanode and electrolyte interface.

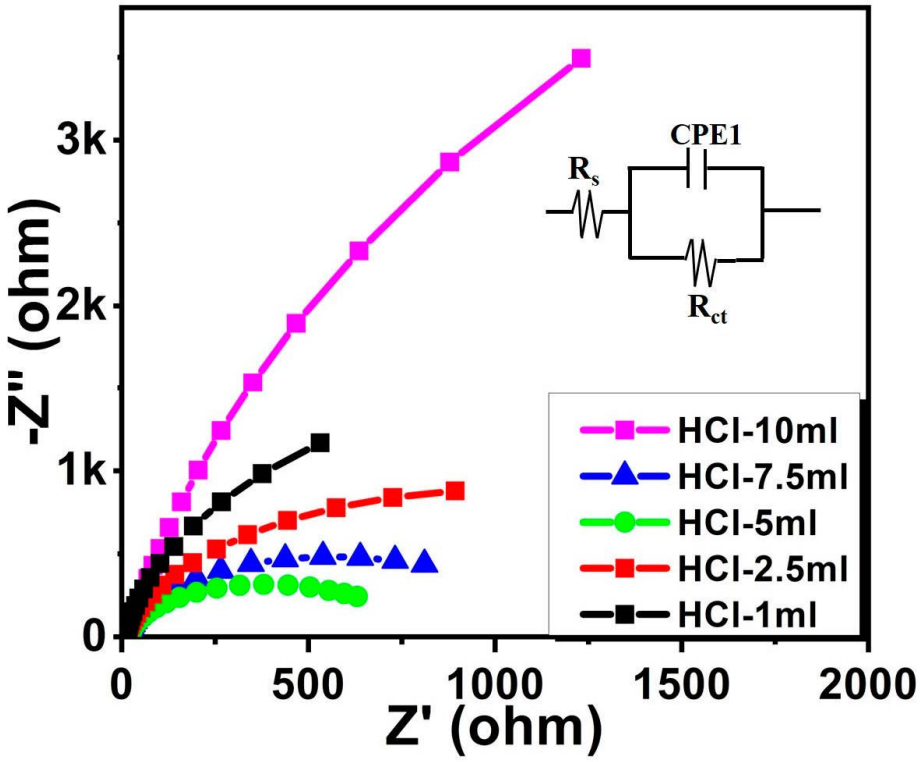

Figure 8. EIS Nyquist plots of all the photoanodes under AM 1.5 G conditions. (Inset: the equivalent circuit model).

4. Conclusions

In summary, we demonstrated the influence of the precursor solution's pH level on the structural evolution, crystal growth, and nucleation of $WO_3 \cdot nH_2O$ and WO_3 nanostructures. The XRD and FTIR results on $WO_3 \cdot nH_2O$ verified that the quantity of hydrate groups increased due to the interaction of H^+ and water molecules with an increasing HCl volume. Surface analyses using AFM and SEM confirmed that the evolution of grain size, surface roughness, and grain growth on $WO_3 \cdot nH_2O$ and WO_3 nanostructures were affected by the precursor solution's pH value. The photoelectrochemical performance confirmed that the best photocurrent density and charge transfer resistance were obtained using the HCl-5 mL sample due to its structural benefits, which facilitated efficient charge transfer and ion diffusion between the photoanode and the electrolyte. Our findings offer a facile approach to obtaining superior performance in PEC water splitting.

Supplementary Materials: The following supporting information can be downloaded at: https://www.mdpi.com/article/10.3390/nano14010008/s1, Figure S1: Schematics of the preparation procedures of $WO_3 \cdot nH_2O$ and WO_3 materials. Figure S2: Illustrations of the preparation procedures of WO_3 photoanode on FTO substrate. Figure S3: XRD spectra of the $WO_3 \cdot nH_2O$ powders obtained by acid precipitation process with 2theta range from 10° to 70°. (a) HCl-1 mL, (b) HCl-2.5 mL, (c) HCl-5 mL, (d) HCl-7.5 mL, (e) HCl-10 mL samples. Figure S4: XRD spectra of the WO_3 nanoplates grown on FTO glass with different HCl volume. (a) HCl-1 mL, (b) HCl-2.5 mL, (c) HCl-5 mL, (d) HCl-7.5 mL, (e) HCl-10 mL samples. Figure S5: LSV curves obtained from the WO_3 photoanodes under AM 1.5G condition. (a) HCl-1 mL, (b) HCl-2.5 mL, (c) HCl-5 mL, (d) HCl-7.5 mL, (e) HCl-10 mL samples. Figure S6: EIS Nyquist plots of all the photoanodes under AM 1.5G condition. (a) HCl-1 mL, (b) HCl-2.5 mL, (c) HCl-5 mL, (d) HCl-7.5 mL, (e) HCl-10 mL samples.

Author Contributions: Conceptualization, S.-H.B. and S.-J.Y.; methodology, S.-H.B.; software, S.-H.B.; validation, S.-H.B. and S.-J.Y. and D.K.; formal analysis, S.-J.Y.; investigation, S.-H.B.; resources, S.-J.Y.; data curation, S.-J.Y. and D.K.; writing—original draft preparation, S.-H.B. and S.-J.Y.; writing—review and editing, S.-H.B.; visualization, S.-J.Y. and D.K.; supervision, S.-H.B.; project administration, S.-H.B.; funding acquisition, S.-H.B. All authors have read and agreed to the published version of the manuscript.

Funding: This work was supported by the National Research Foundation of Korea (NRF) grant funded by the Government of the Republic of Korea (MSIT) (No. 2023R1A2C1004725 and No. RS-2023-00236572). And, the present research was supported by the research fund of Dankook University in 2023 (Outstanding Junior Faculty Researcher Support Program).

Data Availability Statement: The data presented in this study are available on reasonable request from the corresponding author.

Conflicts of Interest: The authors declare that there are no conflict of interest.

References

1. Armaroli, N.; Balzani, V. The future of energy supply: Challenges and opportunities. *Angew. Chem. Int. Ed.* **2007**, *46*, 52. [CrossRef] [PubMed]
2. Chen, X.; Li, C.; Grätzel, M.; Kostecki, R.; Mao, S.S. Nanomaterials for renewable energy production and storage. *Chem. Soc. Rev.* **2012**, *41*, 7909. [CrossRef] [PubMed]
3. Hosseini, S.E.; Wahid, M.A. Hydrogen production from renewable and sustainable energy resources: Promising green energy carrier for clean development. *Renew. Sustain. Energy Rev.* **2016**, *57*, 850. [CrossRef]
4. Nikolaidis, P.; Poullikkas, A. A comparative overview of hydrogen production processes. *Renew. Sustain. Energy Rev.* **2017**, *67*, 597. [CrossRef]
5. Møller, K.T.; Jensen, T.R.; Akiba, E.; Li, H.-W. Hydrogen—A sustainable energy carrier. *Prog. Nat. Sci.* **2017**, *27*, 34. [CrossRef]
6. Kim, J.H.; Hansora, D.; Sharma, P.; Jang, J.W.; Lee, J.S. Toward practical solar hydrogen production—An artificial photosynthetic leaf-to-farm challenge. *Chem. Soc. Rev.* **2019**, *48*, 1908. [CrossRef] [PubMed]
7. Ye, S.; Ding, C.; Liu, M.; Wang, A.; Huang, Q.; Li, C. Water oxidation catalysts for artificial photosynthesis. *Adv. Mater.* **2019**, *31*, 1902069. [CrossRef] [PubMed]
8. Kuti, L.M.; Bhella, S.S.; Thangadurai, V. Transformation of proton-conducting perovskite-type into fluorite-type fast oxide ion electrolytes using a CO_2 capture technique and their electrical properties. *Inorg. Chem.* **2009**, *48*, 6804. [CrossRef]
9. Gotić, M.; Ivanda, M.; Popović, S.; Musić, S. Synthesis of tungsten trioxide hydrates and their structural properties. *Mater. Sci. Eng. B* **2000**, *77*, 193. [CrossRef]
10. Jiao, Z.; Wang, J.; Ke, L.; Sun, X.W.; Demir, H.V. Morphology-tailored synthesis of tungsten trioxide (hydrate) thin films and their photocatalytic properties. *ACS Appl. Mater. Interfaces* **2011**, *3*, 229. [CrossRef]
11. Amano, F.; Tian, M.; Wu, G.; Ohtani, B.; Chen, A. Facile preparation of platelike tungsten oxide thin film electrodes with high photoelectrode activity. *ACS Appl. Mater. Interfaces* **2011**, *3*, 4047. [CrossRef] [PubMed]
12. Nayak, A.K.; Sohn, Y.; Pradhan, D. Facile green synthesis of $WO_3 \cdot H_2O$ nanoplates and WO_3 nanowires with enhanced photoelectrochemical performance. *Cryst. Growth Des.* **2017**, *17*, 4949. [CrossRef]
13. Mitchell, J.B.; Lo, W.C.; Genc, A.; Lebeau, J.; Augustyn, V. Transition from Battery to Pseudocapacitor Behavior via Structural Water in Tungsten Oxide. *Chem. Mater.* **2017**, *29*, 3928. [CrossRef]
14. Zhou, J.; Lin, S.; Chen, Y.; Gaskov, A.M. Facile morphology control of WO_3 nanostructure arrays with enhanced photoelectrochemical performance. *Appl. Surf. Sci.* **2017**, *403*, 274. [CrossRef]
15. Nayak, A.K.; Lee, S.; Choi, Y.I.; Yoon, H.J.; Sohn, Y.; Pradhan, D. Crystal phase and size-controlled synthesis of tungsten trioxide hydrate nanoplates at room temperature: Enhanced Cr(VI) photoreduction and methylene blue adsorption properties. *ACS Sustain. Chem. Eng.* **2017**, *5*, 2741. [CrossRef]

16. Zheng, G.; Wang, J.; Liu, H.; Murugadoss, V.; Zu, G.; Che, H.; Lai, C.; Li, H.; Ding, T.; Gao, Q.; et al. Tungsten oxide nanostructures and nanocomposites for photoelectrochemical water splitting. *Nanoscale* **2019**, *11*, 18968. [CrossRef] [PubMed]
17. Zhang, W.; Chen, H.; Peng, Q.; Liu, X.; Dian, L.; Ye, W.; Chang, Y.; Ma, X.; Wang, H. Controlled fabrication of WO_3 nanoplate films and its photoelectrochemical properties. *Mater. Res. Express.* **2019**, *6*, 095901. [CrossRef]
18. Pham, N.L.; Luu, T.L.A.; Nguyen, H.L.; Nguyen, C.T. Effects of acidity on the formation and adsorption activity of tungsten oxide nanostructures prepared via the acid precipitation method. *Mater. Chem. Phys.* **2021**, *272*, 125014. [CrossRef]
19. Liang, F.; Lin, Y.; He, Z.; Chen, W.; Zhu, Y.; Chen, T.; Liang, L.; Ma, S.; Wu, Y.; Tu, B.; et al. Promising ITO-free perovskite solar cells with WO_3-Ag-SnO_2 as transparent conductive oxide. *J. Mater. Chem. A* **2018**, *6*, 19330. [CrossRef]
20. Yadav, S.; Lohia, P.; Sahu, A. Enhanced performance of double perovskite solar cell using WO_3 as an electron transport material. *J. Opt.* **2023**, *52*, 776. [CrossRef]
21. Farhadian, M.; Sangpout, P.; Hosseinzadeh, G. Morphology dependent photocatalytic activity of WO_3 nanostructures. *J. Energy Chem.* **2015**, *24*, 171. [CrossRef]
22. Park, M.; Seo, J.H.; Song, H.; Nam, K.M. Enhanced visible light activity of single-crystalline WO_3 microplates for photoelectrochemical water oxidation. *J. Phys. Chem. C* **2016**, *120*, 9192. [CrossRef]
23. Ahmed, B.; Kumar, S.; Ojha, A.K.; Donfack, P.; Materny, A. Facile and controlled synthesis of aligned WO3 nanorods and nanosheets as an efficient photocatalyst material. *Spectrochim. Acta Part A Mol. Biomol. Spectrosc.* **2017**, *175*, 250. [CrossRef] [PubMed]
24. Ke, J.; Zhou, H.; Liu, J.; Duan, X.; Zhang, H.; Liu, S.; Wang, S. Crystal transformation of 2D tungstic acid H_2WO_4 to WO_3 for enhanced photocatalytic water oxidation. *J. Colloid Interface Sci.* **2018**, *514*, 576. [CrossRef] [PubMed]
25. Zhao, L.; Xi, X.; Liu, Y.; Ma, L.; Nie, Z. Facile synthesis of WO_3 micro/nanostructures by paper-assisted calcination for visible-light-driven photocatalysis. *Chem. Phys.* **2020**, *528*, 110515. [CrossRef]
26. Perfecto, T.M.; Zito, C.A.; Volanti, D.P. Room-temperature volatile organic compounds sensing based on WO3·0.33H2O, hexagonal-WO3, and their reduced graphene oxide composites. *RSC Adv.* **2016**, *6*, 105171.
27. Wang, L.; Hu, H.; Xu, J.; Zhu, S.; Ding, A.; Deng, C. WO_3 nanocubes: Hydrothermal synthesis, growth mechanism, and photocatalytic performance. *J. Mater. Res.* **2019**, *34*, 2955. [CrossRef]
28. Ou, P.; Song, F.; Yang, Y.; Shao, J.; Hua, Y.; Yang, S.; Wang, H.; Luo, Y.; Liao, J. $WO_3 \cdot nH_2O$ crystals with controllable morphology/phase and their optical absorption properties. *ACS Omega* **2022**, *7*, 8833. [CrossRef]
29. Livage, J.; Guzman, G. Aqueous precursors for electrochromic tungsten oxide hydrates. *Solid State Ion.* **1996**, *84*, 205. [CrossRef]
30. Hu, W.-H.; Han, G.-Q.; Dong, B.; Liu, C.-G. Facile Synthesis of Highly Dispersed WO3·H2O and WO3 Nanoplates for Electrocatalytic Hydrogen Evolution. *J. Nanomater.* **2015**, *2015*, 346086.
31. Han, H.; Nayak, A.K.; Choi, H.; Ali, G.; Kwon, J.; Choi, S.; Paik, U.; Song, T. Partial dehydration in hydrated tungsten oxide nanoplates leads to excellent and robust bifunctional oxygen reduction and hydrogen evolution reactions in acidic media. *ACS Sustain. Chem. Eng.* **2020**, *8*, 9507. [CrossRef]
32. Zhang, N.; Chen, C.; Mei, Z.; Liu, X.; Qu, X.; Li, Y.; Li, S.; Qi, W.; Zhang, Y.; Ye, J.; et al. Monoclinic tungsten oxide with {100} facet orientation and tuned electronic band structure for enhanced photocatalytic oxidations. *ACS Appl. Mater. Interfaces* **2016**, *8*, 10367. [CrossRef] [PubMed]
33. Daniel, M.F.; Desbat, B.; Lassegues, J.C.; Gerand, B.; Figlarz, M. Infrared and Raman study of WO_3 tungsten trioxides and WO_3, xH_2O tungsten trioxide tydrates. *J. Solid State Chem.* **1987**, *67*, 235. [CrossRef]
34. Baek, S.-H.; Jeong, Y.-M.; Kim, D.Y.; Park, I.-K. Phase transformation of NiCo hydroxides derived from carbonate anion and its effect on electrochemical pseudocapacitor performance. *Chem. Eng. J.* **2020**, *393*, 124713. [CrossRef]
35. Zheng, J.Y.; Song, G.; Hong, J.; Van, T.K.; Pawar, A.U.; Kim, D.Y.; Kim, C.W.; Haider, Z.; Kang, Y.S. Facile fabrication of WO_3 nanoplates thin films with dominant crystal facet of (002) for water splitting. *Cryst. Growth Des.* **2014**, *14*, 6057. [CrossRef]
36. Bredar, A.R.C.; Chown, A.L.; Burton, A.R.; Farnum, B.H. Electrochemical impedance spectroscopy of metal oxide electrodes for energy applications. *ACS Appl. Energy Mater.* **2020**, *3*, 66. [CrossRef]
37. Kim, J.Y.; Magesh, G.; Youn, D.H.; Jang, J.-W.; Kubata, J.; Domen, K.; Lee, J.S. Single-crystalline, wormlike hematite photoanodes for efficient solar water splitting. *Sci. Rep.* **2013**, *3*, 2681. [CrossRef] [PubMed]
38. Kong, Y.; Sun, H.; Fan, W.; Wang, L.; Zhao, H.; Zhao, X.; Yuan, S. Enhanced photoelectrochemical performance of tungsten oxide film by bifunctional Au nanoparticles. *RSC Adv.* **2017**, *7*, 15201. [CrossRef]